Design optimization of plastic scintillators with wavelength-shifting fibers and silicon photomultiplier readouts in the top veto tracker of the JUNO-TAO experiment

Guang Luo[1] · Y. K. Hor[1] · Pei-Zhi Lu[1] · Zhi-Min Wang[2,3] · Ru-Hui Li[2] · Min Li[2,3] · Yi-Chen Li[2,3] · Liang Zhan[2,3] · Wei Wang[1,4] · Yue-Huan Wei[4] · Yu Chen[1] · Xiang Xiao[1] · Feng-Peng An[1]

Abstract

Plastic scintillators (PSs) embedded with wavelength-shifting fibers are widely used in high-energy particle physics, such as in muon taggers, as well as in medical physics and other applications. In this study, a simulation package was built to evaluate the effects of the diameter and layout of optical fibers on the light yield with different configurations. The optimal optical configuration was designed based on simulations and validated using two PS prototypes under certain experimental conditions. A top veto tracker (TVT) for the JUNO-TAO experiment, comprising four layers of 160 strips of PS, was designed and evaluated. The threshold was evaluated when the muon tagging efficiency of a PS strip was >99%. The efficiency of three layer out of four layer of TVT is >99%, even with a tagging efficiency of a single strip as low as 97%, using a threshold of 10 photoelectrons and assuming a 40% silicon PM photon detection efficiency.

Keywords Plastic scintillator · WLS fiber · Light yield · Optical transmission performance · Muon tagging efficiency · JUNO-TAO

1 Introduction

Collisions between primary cosmic rays and the Earth's atmosphere produce numerous muons [1], the average kinetic energy of which at sea level is several GeV [2]. Because of their high energy, large mass, small deceleration, deflection in the electromagnetic field, and small bremsstrahlung effect with the atomic nuclear electric field in matter, muons have strong penetration power [3]. A subsystem of the muon veto detector with high muon tagging efficiency is very important to greatly reduce the background induced by cosmic-ray (CR) muons for experiments with only limited overburden near the ground, where the flux of muons is normally four to seven orders of magnitude higher than that of underground laboratories with large overburden (e.g., the Jinping underground laboratory [4], Gran Sasso underground laboratory [5], and Canfranc underground laboratory [6]). For example, in neutrino experiments [7–9], dark matter experiments [10–13], and neutrinoless double-beta decay experiments [14–16], muon veto systems require muon tagging efficiencies of >99%. At present, detectors based on plastic scintillators (PSs) have the advantage of

✉ Y. K. Hor
heyuanq@mail.sysu.edu.cn

✉ Zhi-Min Wang
wangzhm@ihep.ac.cn

✉ Wei Wang
wangw223@mail.sysu.edu.cn

1 School of Physics, Sun Yat-sen University, Guangzhou 510275, China

2 Institute of High Energy Physics, Beijing 100049, China

3 University of Chinese Academy of Sciences, Beijing 100049, China

4 Sino-French Institute of Nuclear Engineering and Technology, Sun Yat-sen University, Zhuhai 519082, China

easy machining [17–21], flexible structure design, and efficient and stable performance [22, 23]. PS detectors [24], especially those with wavelength-shifting (WLS) fibers [25–30], and optical photodetectors (multi-anode photomultiplier tubes (PMTs) or silicon photomultipliers (SiPMs)) were used in OPERA [31], MINOS [32], LHAASO [33, 34], and many other experiments [35–38]. PS detectors have several applications in geological imaging [39–42] and reactor monitoring [43–45].

The Taishan Antineutrino Observatory (TAO, or JUNO-TAO) is a satellite experiment at the Jiangmen Underground Neutrino Observatory (JUNO) [8, 9]. The main purpose of the TAO experiment is to provide a precise neutrino energy reference spectrum for the JUNO and benchmark measurements for the nuclear database. The TAO detector system consists of a central detector (CD), outer shielding, and a veto system. The CD was placed ~30 m away from the core of the Taishan Nuclear Power Plant. The CD consists of a 2.8-ton gadolinium-doped liquid scintillator (LS) in a spherical acrylic vessel. As the target material, a gadolinium-doped LS reacts with neutrinos from the reactor to measure the neutrino energy spectrum [46]. Because TAO only has a limited vertical overburden of 4 m of concrete, the major backgrounds for the TAO experiment are muon spallation products and accidental coincidences, mostly from natural radioactivity. The top veto tracker (TVT) requires tag muons with an efficiency of >99%.

The rest of this paper is organized as follows: In Sect. 2, a comparison is made between a simulation based on Geant4 [47–49] and a measurement of a prototype of a PS strip with a WLS fiber readout. The light-yield results of the experiment and simulation were consistent when passing through muons. In Sect. 3, the diameter and the layout of the WLS fiber are further checked for higher light yield against the simulation. An optimized design of the PS strip with WLS fibers and a SiPM readout is proposed for the TVT system of JUNO-TAO with a high light yield and high muon tagging efficiency; this will provide good reference and guidance for the design of a PS detector with WLS fiber. Simultaneously, the reliability of the optimal design is preliminarily verified experimentally. In Sect. 4, with the proposed PS strip design, the expected performance of the TAO TVT system is demonstrated. Finally, a summary is presented in Sect. 5.

2 Prototype PS strip with WLS fiber and the simulation

Muons deposit their energy when they pass through and interact with the surrounding materials; the process of muon energy loss is called muon ionization energy loss [3]. The average energy loss per distance (mass thickness) can be described by the Bethe–Bloch formula [3, 50]

$$-\frac{dE}{dx} = Kz^2 \frac{Z}{A} \frac{1}{\beta^2} \left[\frac{1}{2} \ln \left(\frac{2m_e c^2 \beta^2 \gamma^2 W_{max}}{I^2} \right) - \beta^2 - \frac{\delta}{2} \right], \quad (1)$$

where K is a constant; z is the unit charge of the incident muon; m_e and c are the electron mass and speed of light, respectively; Z and A are the atomic and mass numbers, respectively, of the passing-through matter; W_{Max} is the maximum kinetic energy transferred to an electron when a muon collides with an atom; I is the average excitation energy of the matter; β is the ratio of the speed of a particle to that of light; γ denotes the Lorentz factor; and δ is a correction factor for the density effect of matter. The above parameters are constant for any given matter.

From Eq. (1), the deposited energy of a muon in the material is related to the muon's energy and the atomic number of the material. For thin-layer media with an atomic number of <20, such as a PS strip, muons pass through almost in straight lines. The partially lost energy of the muon is converted into light in the PS strip, and the light is exported by the WLS fiber, where SiPMs coupled with the fiber are an effective, convenient, and rapid method to pick up photons and then convert them into an electrical signal.

A prototype of a PS with a WLS fiber readout was designed and fabricated, as shown in Fig. 1 [51] (designated as Option 1). Its size was 2 m (length) × 0.1 m (width) × 0.02 m (thickness), and four optical fibers with diameters of 1 mm were used. The pink lines represent the WLS fibers equally spaced, inserted, and filled on the surface of the PS strip. The length of the straight portion was 1.9 m. The arrangement was symmetrical in both the length and width directions. Two of the fibers were focused into a single group, which could be coupled with optical sensors. This option can reduce the number of optical sensors required. For example, four SiPMs (red circular points in the figure) can be used for each fiber group or two PMTs can be used for each PS end. Finally, the PS was wrapped in a reflective film
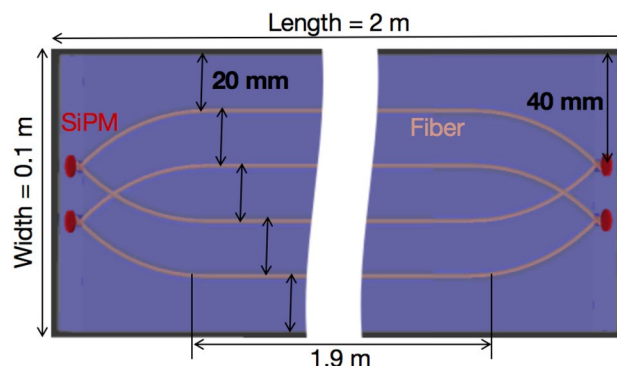

Fig. 1 (Color online) Design of a prototype of the PS strip with WLS fiber (option 1)

(aluminum foil), except for the pipes of the optical fiber, to export photons. Additional details can be found in Ref. [51]. The prototype was tested using a CR muon before design optimization.

A CR muon survey along the length of the PS strip prototype with the PMT/SiPM was performed using the scheme shown in Fig. 2 (in which the arrangement of the optical fibers is not shown). The CR muon [28, 52] was selected using two scintillators placed on the prototype as a monitor. When the CR muon monitors were triggered, the signals of the PS strip were also recorded. Nine points equally spaced along the strip were measured relative to the center of the PS. Further details of the experiment can be found in Ref. [51]. The PS strip was fabricated by the Beijing Hoton Nuclear Technology Co., Ltd. [53]. The type of fiber used was the WLS fiber BCF92 [54, 55]. For further understanding and optimization, a Monte Carlo (MC) simulation project was set up based on Geant4 [47, 49, 52] with the parameters provided by the manufacturers of the PS, reflective film, and WLS fiber [55, 56]. The simulation project mainly comprised three parts. The first part is the detector geometry, and the PS geometry with optical fibers was designed through a geometric interface. This is why various geometric designs exist in the subsequent optimizations. The second is the physical process section, which contains a physical list and the optical processes of optical photons. The physical list included ionization, bremsstrahlung, multiple scattering, pair generation, Compton scattering, and photoelectric effects. The optical processes included the generation of scintillation and Cherenkov light, wavelength-shift effects, Rayleigh scattering, bulk absorption, and boundary processes. The third step is the extraction and analysis of information. The PS and PMT/SiPM were set as sensitive areas. The PS was responsible for obtaining information about the muon, and the PMT/SiPM was responsible for obtaining information about the photon hitting. A parameter interface was provided in the simulation package to determine the properties of the material, such as the PS attenuation length, the scintillator yield (referring to the number of photons generated when the energy deposited

in the scintillator is 1 MeV), and the reflectivity of reflective film. By scanning these parameters, a series of simulation responses can be obtained. These included the light yield along the PS longitudinal direction, which is the photoelectron (p.e.) count taking in consideration the corresponding photon detection efficiency (PDE) of the SiPM or quantum efficiency (QE) of the PMT. χ^2 analysis was performed using the experimental data. Table 1 lists the parameters corresponding to the minimum χ^2. In the subsequent optimization, the parameters of the PS, optical fiber, and reflective film in Table 1 are the same as those in the simulation.

A comparison of the measured light yield and that of the simulation at different positions is shown in Fig. 3a, where the light yield (in p.e.) refers to the average value of the photoelectron distribution of the selected muons hitting each position, and the x-axis represents the distance from the center of the PS strip in the length direction. When using the PMT as the sensor, the simulation and data were in good agreement within the error. The light yield at both ends was symmetrically distributed around the center of the PS. Owing to the different QEs of the PMT, the light yields at the two ends were not strictly symmetrical. The distribution of light yield at one end when using a SiPM of the same type as the sensor is shown here. As shown in the figure, the light yield of the SiPM was greater than that of the PMT. Based

Table 1 Key parameters used in the simulation of the PS strip prototype

Material	Property	Parameter
PS	Base	Polyvinyltoluene
	Scintillation yield (photons/MeV)	8000
	Emission peak (nm)	415
	Attenuation length (cm)	200 @ 400 nm
WLS fiber	Core	Polystyrene
	Attenuation length (cm)	380 @ 400 nm
Reflective film	Base	Aluminum
	Reflectivity	85%
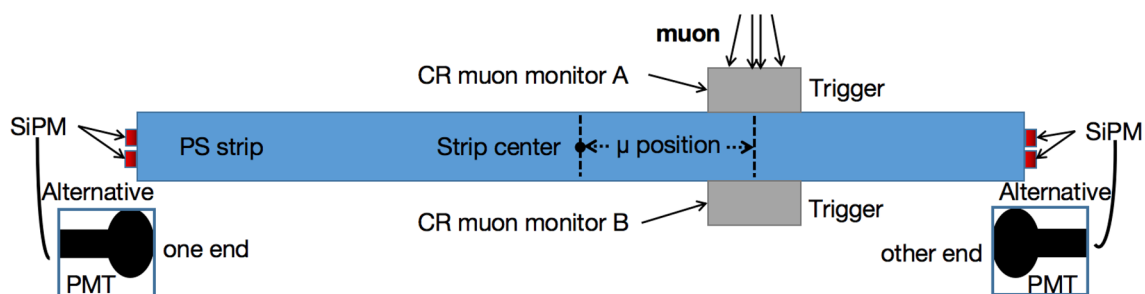
Fig. 2 (Color online) Device and principal diagram for CR muon measurement with the PS strip prototype. The CR muon will be selected by the two muon monitors consisting of small scintillators at different hitting locations. When the CR muon monitors are triggered, the signals of the PS strip will be recorded too

(a)

(b)
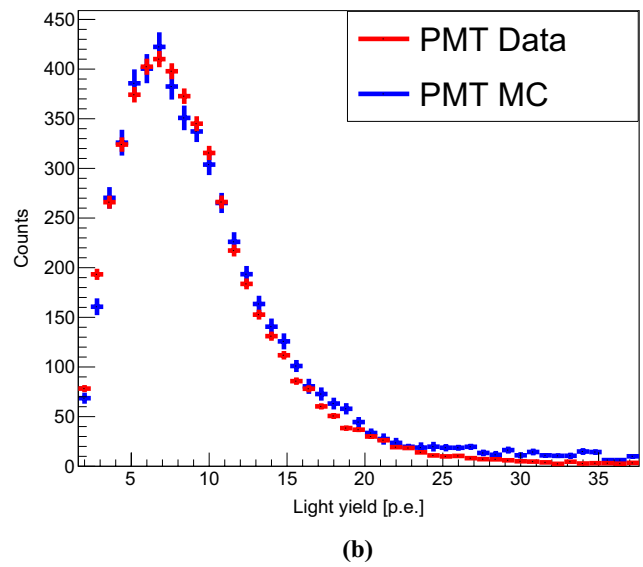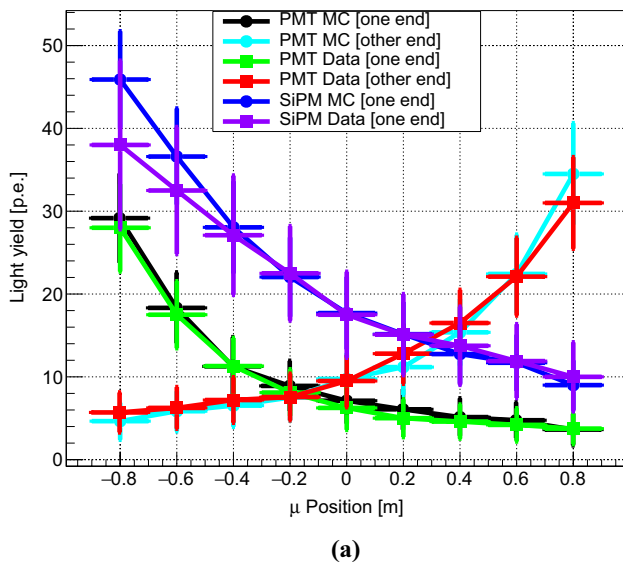
Fig. 3 (Color online) **a** Comparison of the light yield between measurement and simulation at different muon hitting positions. The horizontal error bar is from the dimension of the muon monitors, and the vertical error bar in the MC simulation is the statistical error. Because of the different QEs of PMTs and coupling, the light yield at the two ends is not strictly symmetrical. The light yield of the SiPM is greater than that of the PMT. Based on the SiPM's advantages of compact requirements, robustness, and greater light yield, it is proposed as the sensor for the TVT. **b** Comparison diagram of the experimental energy spectrum and simulation of the PMT at one end when the CR muon monitor is in the center of the PS

on the advantages of compactness, robustness, and higher light yield than the PMT, the SiPM was proposed as sensors for the TVT. In addition to the initial comparison shown in Fig. 3a, another similar comparison of the energy spectra is also obtained between the measurement and simulation at the center of the PS shown in Fig. 3b; except for individual energy points that do not conform to the experiment, others are in good agreement with the experiment within the error range. From an experimental perspective, each PMT has a different QE or each SiPM has a different PDE. Because the following optimization work does not focus on the impact of electronics, in subsequent studies, the QE of each PMT or the PDE of the SiPM will be input with the same value.

3 Optimization of the PS strip layout

Based on the agreement between the experiment and simulation, a further study on the configuration of the PS strip design was performed, addressing the effects of diameter and arrangement of the WLS fiber on the light yield and tagging efficiency. The relationship between the light yield and fiber diameter is shown in Fig. 4 for two PS configurations with the same number of embedded fibers. Each point refers to the light yield of the muon striking the PS center. The magenta heart represents the measurement of the prototype with the PMT mentioned earlier. The simulated relationship between the light yield and fiber diameter is represented by
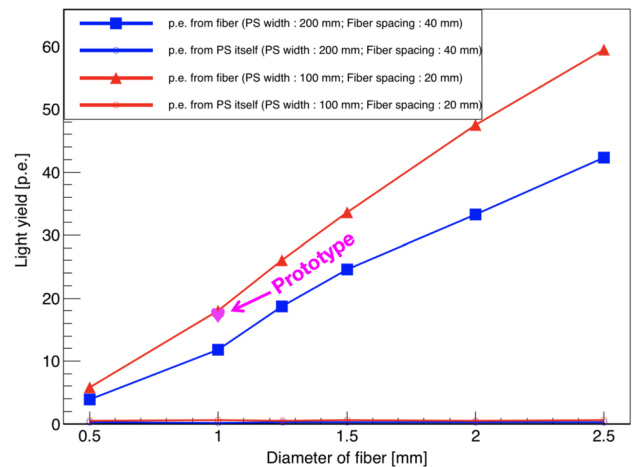
Fig. 4 (Color online) Light yield under the assumption of 30% PDE of SiPM or QE of PMT. Each point refers to the light yield of a muon hitting the PS center. The magenta heart represents the measurement of the prototype with the PMT mentioned earlier. Two widths of 200 and 100 mm for the PS are checked with the same length of 2 m and thickness of 0.02 m. The simulated relationship between the light yield and the fiber diameter is represented by red lines with a spacing of ~20 mm between neighboring fibers. The blue lines represent the simulated relationship with a spacing of ~40 mm between neighboring fibers. The same four fibers are used in each case, which is why the light yield of the 200-mm-wide PS is less than that of the 100-mm one

red lines with a PS width of 100 mm and a spacing of ~ 20 mm between neighboring fibers. The blue lines represent the simulated relationship with a PS width of 200 mm and a spacing of ~40 mm between neighboring fibers. Most photons are collected through the WLS fibers using sensors. Because the area of the optical sensor is larger than the dimensions of the optical fiber, there are still some PS scintillation photons directly collected by the sensors that do not pass through the WLS fiber. The two straight lines at the bottom represent the photons passing directly from the PS to the SiPM, where the light yield contributed by the PS itself is independent of the fiber diameter.

According to the trend observed in the plot, the larger the fiber diameter or the smaller the spacing of the neighboring fibers, the higher the light yield. Finally, a 1.5-mm fiber diameter is suggested based on the expected response and reasonable cost.

Following the requirements of the JUNO-TAO TVT system, a PS strip with a width of 20 cm is suggested based on the fabrication, electronics, and cost. However, there

remain more than one option proposed following a different strategy, as shown in Fig. 5. The length and thickness of all options were 2 m and 20 mm, respectively. The widths of options 2, 3, 3-1, and 4 were 200 mm, whereas that of option 1 was only 100 mm, as in the measured prototype. The eight fibers had a similar spacing of 20 mm, except for option 1. The fibers of option 2 were arranged only on the front of the PS, numbering twice that of option 1. Option 3 was similar to option 2, but with four optical fibers installed on the back and another four on the front of the PS. The fiber layouts of options 3-1 and 4 were arranged differently. The fibers of options 3-1 were more uniform than those of option 2 but were not as staggered as those of option 4. For options 1, 2, and 3, the length of the straight portion of the fibers was 1.9 m. For options 3-1 and 4, the length of the straight portion of the fibers was 1.5 m.

The PS width and WLS fiber diameter for all options are listed in Table 2. The performance (mainly light yield and muon tagging efficiency) and differences among the proposed methods were further evaluated by performing
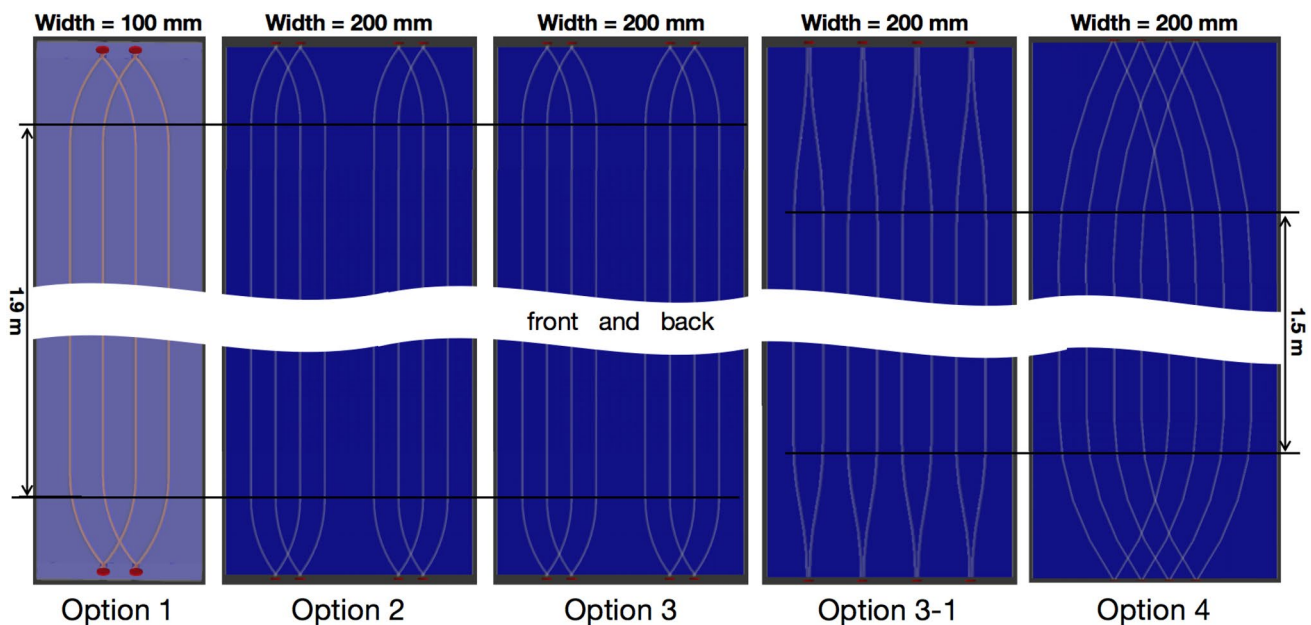
Fig. 5 (Color online) All evaluated designs of a single PS strip. The number of fibers is eight with a similar spacing except for option 1. The fibers for option 2 are only arranged on the front of the PS as doubled that of option 1. Option 3 is similar to option 2, but with four optical fibers installed on the back and another four on the front of the PS, respectively. The fiber layout of options 3-1 and 4 is in a different arrangement. The fibers of options 3-1 are more uniform than those of option 2, but they are not staggered like that of option 4

Table 2 Main configurations of different options of PS strip layout

Configuration	Option 1	Option 2	Option 3	Option 3-1	Option 4
PS width (mm)	100	200	200	200	200
Fiber numbers	4	8	8	8	8
Fiber diameter (mm)	1	1.5	1.5	1.5	1.5
Fiber spacing (mm)	20	20	20	24	22.5

simulations. They can be divided into three categories for comparative study:

Option 2 versus option 3   addresses the dependence of light yield on fiber placement.

Option 2 versus option 3-1 addresses the basic dependence of light yield on the uniformity of the fiber arrangement in the PS.

Option 2 versus option 4   addresses the dependence of light yield on the fiber layout.

3.1 Light yield

The angular distribution of CR muons hitting the PS affects the PS response. To verify the difference and eliminate the additional influence of angular dependence, muons that were vertically and uniformly incident on the PS strip were used in the simulation. The results for the number of photons received by the SiPM for option 1–4 are shown in Fig. 6a. The X-axis represents the number of photons, nPhotons (where light yield = nPhotons × PDE), which is the sum of the photons collected by all the SiPMs in a muon event. The figure also shows the average number of photons received by all SiPMs for all muon events. The black line represents the distribution of photons collected by the SiPM under option 1. The red and green lines represent the photon number distributions of options 2 and 3, which overlap, indicating that the back or front locations of the fibers have no obvious effect on the collection of photons. The photons received by the fiber are from absorption and reemission and from reflection of the Cerenkov photons of the PS rather than directly generated photons. The average value of nPhotons for option 2 was almost twice that for option 1. Option 4 has a greater

nPhotons than those of the previous three options, indicating that the arrangement of the fibers has a significant impact on the light yield. The difference in nPhotons between options 4 and 2 is studied in detail in Sect. 3.2. All the plots have the same entries; therefore, the maximum height of the plots can be related to the distribution width.

To further evaluate the differences between options 2, 3-1, and 4, more realistic simulations were conducted. The muon generator was updated in terms of the energy and angular distribution according to Refs. [57, 58] as a more realistic situation to model the response of the PS strip. The results are presented in Fig. 6b. The black, blue, and red lines represent the total photon number distributions for options 2, 3-1, and 4, respectively. The figure also shows the average number of photons received by all SiPMs for all muon events. Except for the total number of photons, the average number of photons for option 4 was the highest, option 3-1 was in the middle, and option 2 was the lowest. Option 4 exhibits the best ability to collect photons.

From Eq. (1), it can be observed that the deposited energy is directly proportional to the track length of muons passing through the material. Because of the oblique incidence of muons in the updated muon generator in the second simulation, the track length of the muons in the PS strip can be either less than (representing an edge event) or greater than the thickness of the PS strip. The total photon number in Fig. 6b is much higher than that in Fig. 6a, even for the same option; the average value of nPhotons nearly doubles, whereas some signals with small amplitudes appear. The upper left, upper right, and bottom left panels of Fig. 7 show two-dimensional diagrams of the total photon number versus muon track length for options 2, 3-1, and 4, respectively. Colors in the three panels represent event densities.

(a)

(b)
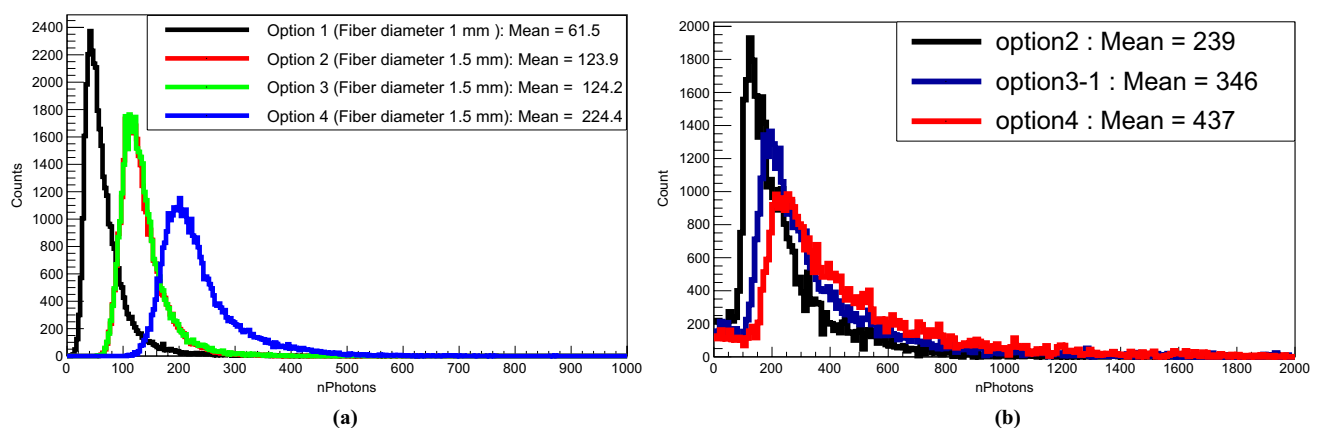
Fig. 6 (Color online) **a** Distribution of total number of photons received by the SiPM for four different options of PS strip layout in the vertical incident muon simulation. nPhotons are the number of photons collected by all the SiPMs in a muon event, without consideration of the corresponding PDE of the SiPM. Light yield = nPhotons × PDE. The average value of nPhotons in option 2 is almost

twice that of option 1. Option 4 has more nPhotons than the previous three options. **b** Distribution of the total number of photons collected by the SiPM with different fiber arrangements under a realistic muon simulation. The black, blue, and red lines represent the total photon number distributions of options 2, 3-1, and 4, respectively
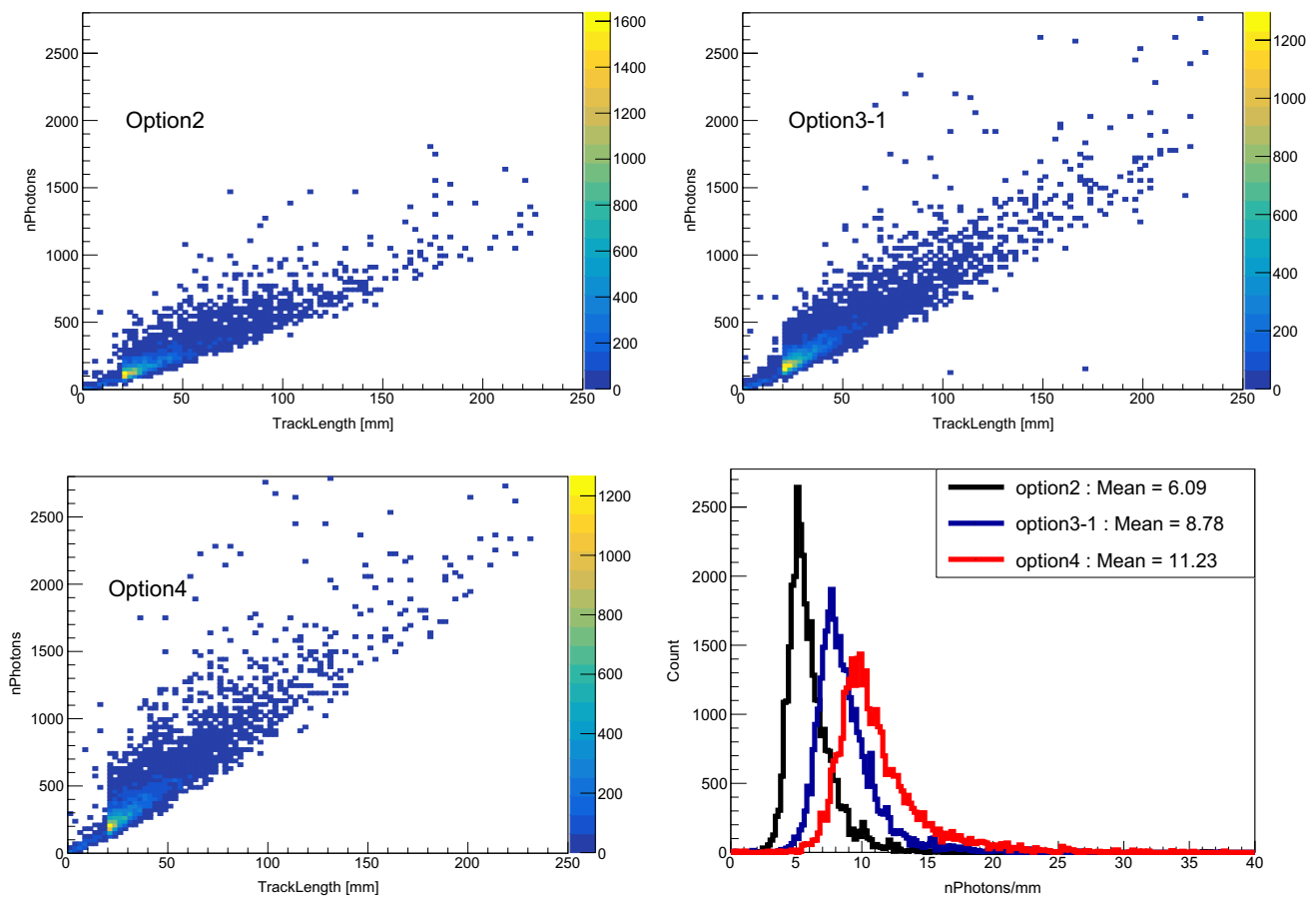
Fig. 7 (Color online) Total photon number versus muon track length. The upper left, upper right, and bottom right panels represent the two-dimensional diagram of total photon number versus muon track length for options 2, 3-1, and 4, respectively. The bottom right shows a comparison of the photon number normalized to unit muon track length

As expected, the total photon number is proportional to the track length. When the track length was 20 mm (i.e., thickness of the PS), the event density was the highest because of the maximum flux density when muons were incident vertically. The bottom right panel of Fig. 7 shows the number of photons per millimeter of muons passing through the PS strip for the three options. The average number of photons per unit length (mm) for option 4 was 11.23, which was nearly twice that of option 2. This indicates that option 4 is the most effective for the light-yield response to a muon when the muon deposits the same amount of energy.

3.2 Transmission performance

Options 2 and 4 have a similar configuration for WLS fiber number and PS length, width, and thickness, but their light yields exhibit an obvious difference. The photon transmission process was further checked for a better understanding of the specific reasons for the influence of the fiber arrangement on the light yield for further optimization.

Muons deposit energy along their tracks in the PS and emit photons in 4π directions. Meanwhile, the photons in the PS propagate through attenuation, absorption, and reemission effects; therefore, accurately characterizing the light transmission performance of different options is complicated. A specified optical survey was conducted to check the photon reflection times before absorption by the WLS fibers of each photon generated by the PS. We tried to cover the center and edge of the PS strip, and the survey locations are shown in Fig. 8. The orange points represent the specified locations for the generation of optical photons. At each point, 15,000 photons were generated in 4π directions to mimic random photons excited by a muon. It is obvious that, before the photons enter the fiber, the more the times of reflection, the more difficult it is for photons to reach the SiPM (an inverse relationship). Simultaneously, if the number of photons entering the fiber is greater, the number of photons arriving at the SiPM is greater (a proportional relationship). To model the combination of these two factors, an *R*-value was proposed as the total number of photons entering the fiber divided by
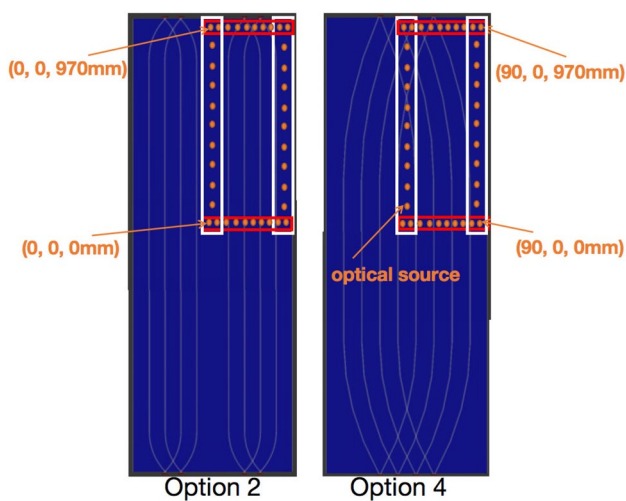
Fig. 8 (Color online) Position distribution diagram of optical scanning for options 2 and 4. The two white frames indicate the simulated points of 11 different positions along the length direction of the PS, respectively. The two red frames indicate the simulated points of 10 different positions along the width direction of the PS, respectively. All points are equidistant from each other

the average number of photon reflections before entering the fiber.

Figure 9 shows the distribution of *R*-values of an optical survey at different positions for options 2 and 4. The abscissa of each point is the position corresponding to the dashed # symbol in the figure, and the specific location is shown in combination with that in Fig. 8. The ordinate of each point is the *R*-value, which represents the optical transmission performance. The red line is the *R*-value of option 4, and the black line represents option 2. The upper left panel of the figure shows the distribution of the *R*-values along the length of the PS strip when the position is at the center of the width of the PS. The *R*-value of option 4 was higher than that of option 2 for the entire length. The lower left panel shows the distribution of the *R*-values along the length of the PS strip when the position was at the edge of the width of the PS strip. The *R*-values of the two options were nearly the same, except for the edge in the length direction, where the *R*-value of option 2 was greater than that of option 4. The upper right panel shows the distribution of the *R*-value along the width direction of the PS when the position is at the center of the PS length, where options 4 and 2 exhibit a trade-off trend. The lower right panel shows the distribution of the *R*-value along the width direction of the PS when the position is at the edge of the length direction of the PS, and the *R*-value of option 4 is greater than that of option 2 at positions within 30 mm from the middle of the width direction of the PS.

The results showed that, when a photon was generated at a location where the fibers were sparse, the number of photons entering the optical fiber decreased sharply, whereas the number of reflections increased. When photons were generated in dense areas of fibers, the number of photons entering the fiber increased dramatically, while the number of reflections decreased dramatically.

Comparison of the four figures from a global perspective reveals that, with the option 2 configuration, the maximum vertical coordinate of the black point is <200, but, with the option 4 configuration, the ordinate of the red point can be >200. The *R*-values of options 4 and 2 exhibit a trade-off trend, and the overall difference is small from the lower left and upper right panels of Fig. 9. The *R*-values of options 4 and 2 differ significantly from those in the upper left and lower right panels of Fig. 9. The distribution of the *R* values in the PS region was obtained. To obtain a quantitative relationship between the optical transmission performance under options 2 and 4 in the entire region, an explanation of mathematical integration (*R*-value) was provided. The integrated areas under the red and black lines in the upper left and lower right panels of Fig. 9 were calculated. The integral area of the red line in the upper left panel was then multiplied by the area in the lower right panel to obtain the transmission performance of the entire region of option 4. The same procedure was followed for the black and red lines, and the product of the two integral areas was used as the transmission performance for the entire region of option 2. Finally, the product of the integral area of the red line was divided by the product of the black line, and the ratio was 2.21. This indicates that the transmission performance of the entire area of option 4 is a factor of 2.21 better than that of option 2. Therefore, it can be understood why the overall photon number of option 4 is greater than that of option 2. At the same time, the curve shows that the *R*-value distribution range of option 4 is greater than that of option 2, which means that the optical export uniformity of option 4 is worse than that of option 2. This is the result of an uneven optical fiber layout. In summary, if the optical fibers in the middle region have a higher density, the final effective light yield will be higher. Therefore, to achieve higher light yield, one should place as many optical fibers as possible in the middle of the PS.

To date, in terms of light yield, many simulations have been performed, and the best configuration has been obtained, that is, option 4, under the current design conditions. To some extent, the reason why it is the best option has been quantitatively explained, and good reference and guidance suggestions for processing technology and structural design were provided. For a PS detector, the most important factor, in addition to the light yield, is the muon tagging efficiency. In the next section, muon tagging efficiency and inefficiency are discussed.
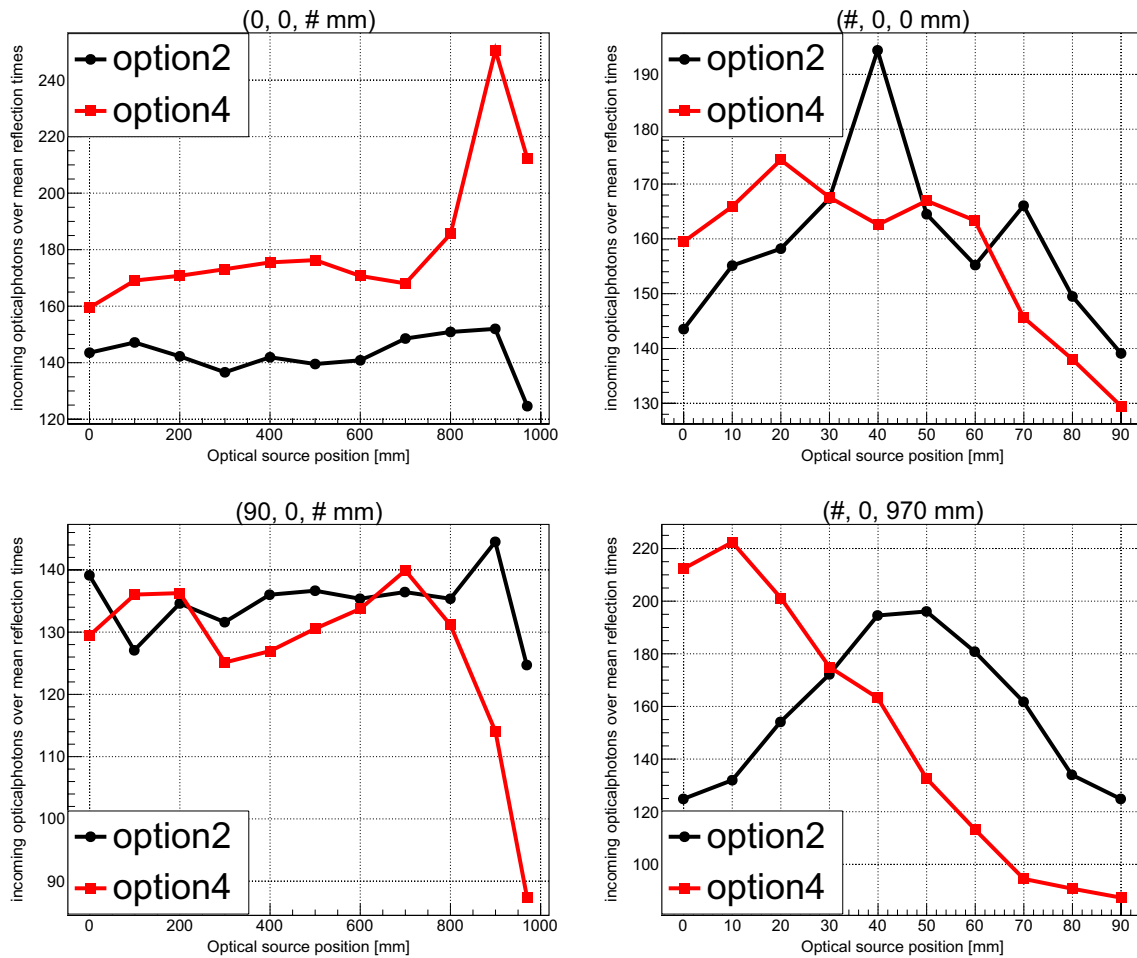
Fig. 9 (Color online) Distribution of the ratio of the photon numbers entering the fiber to the average times of reflections at different positions in the optical survey
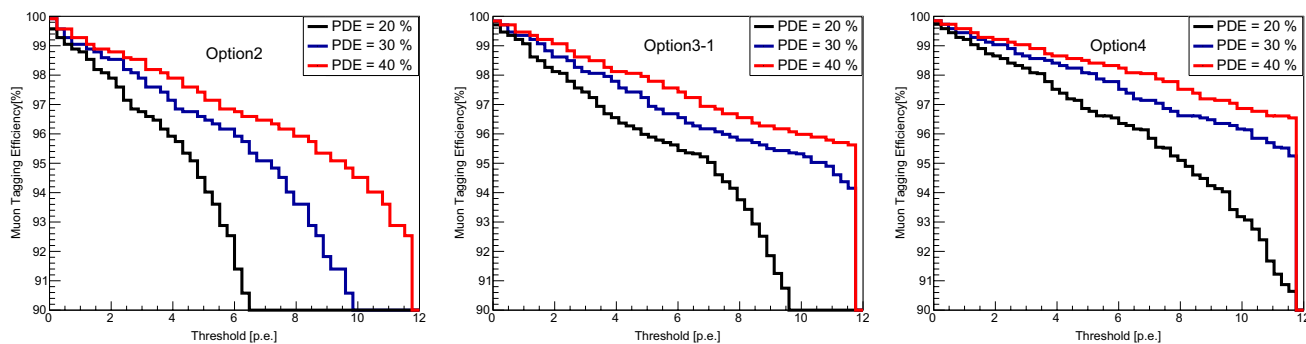
3.3 Muon tagging efficiency and inefficiency

To simplify the simulation process, the PDE of the SiPM was assumed to be 30%. The sum of the four SiPM outputs at both ends can be acquired under different options to further study muon tagging efficiency.

Figure 10 shows the two-dimensional distribution of the light yield at both ends for options 2, 3-1, and 4 in the
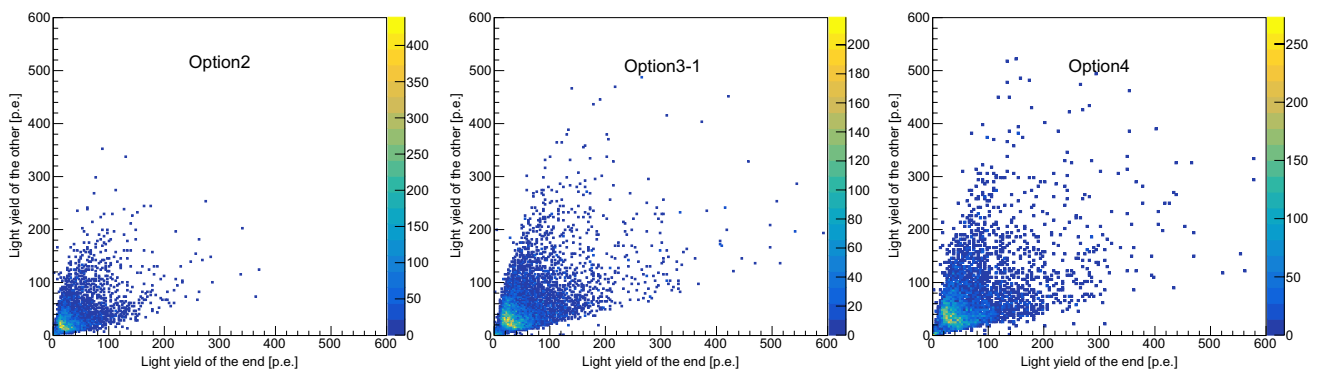
Fig. 10 (Color online) Two-dimensional distributions of light yield at both ends for options 2, 3-1, and 4, respectively, under the assumption of 30% SiPM PDE. The color represents the density of events. From options 2 to 4, the distribution range of light yield gradually widens

Fig. 11 (Color online) Relationship between the muon tagging efficiency and the threshold of options 2, 3-1, and 4, respectively. The threshold represents the sum of the SiPM of each PS end over the threshold individually. As the threshold increases, the muon tagging efficiency of option 4 decreases the least

simulation. The abscissa is the sum of the SiPM outputs at one PS end, and the ordinate is the sum at the other end. The range of light yield at both ends under option 4 was the strongest and most divergent. If the sums at both ends of an event were simultaneously greater than their respective thresholds, the muon was considered to have been detected. The event count of muons hitting the PS strip is denoted by N_{all}, and the event count of detected muons is denoted as N_{tag}. The muon tagging efficiency is defined as the ratio N_{tag}/N_{all}. Here, the environmental background was not considered.

Figure 11 shows the relationship between the muon tagging efficiency and the thresholds of options 2, 3-1, and 4. Black, blue, and red represent the relationship between the efficiency and the threshold when the PDE of the SiPM is 20%, 30%, and 40%, respectively. As shown in the three figures, when the PDE is 20% and the threshold is set to 10, the tagging efficiency of option 4 is still >90%, whereas options 2 and 3-1 have tagging efficiencies of <90%. With an increase in the threshold, the efficiency of option 2 decreased the fastest, followed by that of option 3-1, and option 4 decreased the slowest. According to Fig. 11, the required threshold can be determined when a certain tagging efficiency is achieved.

Figure 12 shows the corresponding threshold when the muon tagging efficiency reached 99% under different PDEs of the SiPM. When the PDE of the SiPM is 40%, for option 2, the threshold cannot exceed 1.5 p.e.; for option 3, it cannot exceed 2.4 p.e.; and for option 4, the threshold can be set to 3 p.e., which significantly reduces the contribution from the SiPM dark noise. Thus far, option 4 is superior to the other options in terms of light yield and muon tagging efficiency. Therefore, option 4 is considered the current optimal configuration. The PDE of the SiPM is therefore set to 40%. The threshold and the corresponding tagging efficiency of a single PS strip when the PDE of the SiPM is 40% are summarized in Table 3.
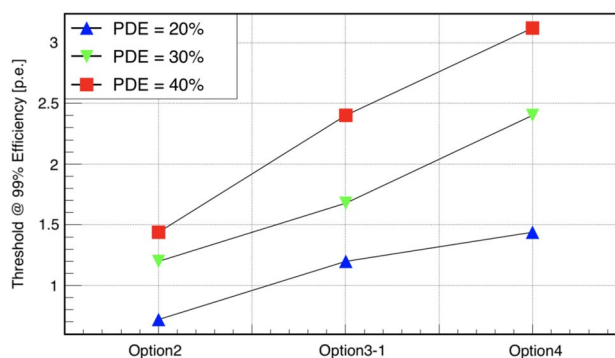

Fig. 12 (Color online) Corresponding threshold limits for options 2, 3-1, and 4, respectively, when the muon tagging efficiency requirement is 99%. When the PDE of the SiPM is 40%, for option 4, the threshold can be set to 3 p.e., which greatly reduces the contribution from dark noise of the SiPM

Table 3 Threshold and corresponding tagging efficiency of a single PS strip with 40% SiPM PDE

Threshold (p.e.)	3.1	6.3	10	15	19
Tagging efficiency	99%	98%	97%	96%	95%

To further verify the simulation, another prototype with option 4 was built, with the parameters of the PS, optical fiber, and reflective film being the same as those before the prototype in the simulation. Only the PDE of the back-end SiPMs was different. Two SiPMs were used as sensors, and an oscilloscope was used to collect the data. The SiPMs used were K-series MicroK-40035-TSV units [59]. The data were saved using a LeCroy HDO4104A oscilloscope. Preliminary experimental results were obtained.
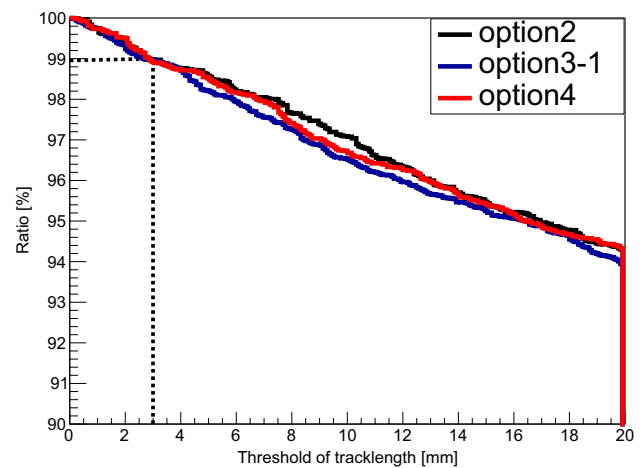
Figure 13 shows the experimental measurement and simulation results from the PS prototype for option 4 when the muon monitor was placed at the PS center. To avoid the
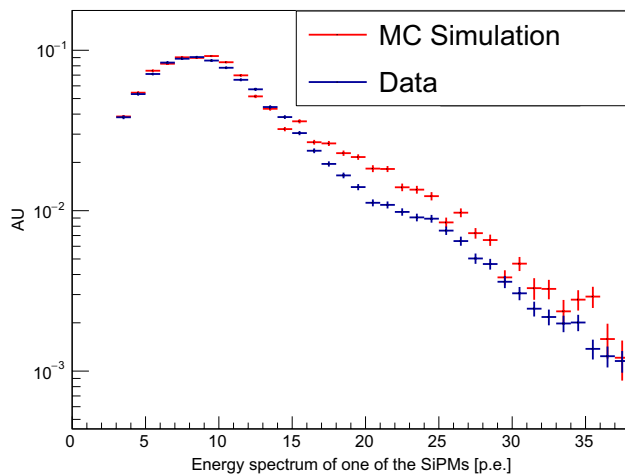
Fig. 13 (Color online) Comparison between the simulation and experiment in terms of the energy spectrum for option 4 with 40% SiPM PDE in the MC simulation. The PDE of the SiPM sample provided by the manufacturer is 46% at a wavelength of 420 nm when the working voltage is 37.2 V. The data are recorded when the CR muon monitor is in the center of PS

Fig. 14 (Color online) Event ratio which the track length of incident muons in the PS strip exceeds the threshold in the total events under options 2, 3-1, and 4, respectively

effects of SiPM dark noise and environmental background, only signals stronger than 3 p.e. were analyzed. The blue line represents the energy spectrum of one SiPM from the measurement. The red line represents the simulation results. Every point has an error bar. The abscissa represents the light yield, and the ordinate represents the log of the normalized event rate. The figure shows that the simulated spectrum nearly corresponds to the experimental spectrum below 12 p.e. The most probable signal amplitude for passing through muons was found to be ~8 p.e. Therefore, for the final configuration used for TAO, where there are four SiPMs at each end of the PS strip, the sum of the most probable signal amplitudes is ~32 p.e. When the spectrum is within the error range of 15–25 p.e., the event rate of the simulated spectrum is greater than that of the experiment. When the spectrum was >25 p.e., the event rates of the simulation and experimental events were relatively low. In the high-energy region, the energy spectrum did not exhibit good consistency, but this did not affect our optimization work. Several main factors lead to differences in the energy spectrum. First, the coupling between the SiPM and the PS is not perfect and is the same for the simulation and measurement. Second, the widths of the two small plastic modules for CR monitors are not the same, which may lead to a deviation of several centimeters in the location where the muon hits, which affects the energy spectrum.

Nevertheless, the light yield under option 4 was much higher than that of option 1 before optimization. This indicates that the proposed optimization method is effective. Based on the above analysis and design, the light yield and

muon tagging efficiency corresponding to options 2, 3-1, and 4 were obtained. When the muon tagging efficiency reached 99%, option 4 had the highest threshold limit.

To study and discuss the inefficiencies of the simulation, the track lengths of all muons in the PS were counted. These inefficiencies can be indirectly explained by the track length distribution.

Figure 14 shows the ratio of muon events whose track length exceeded a certain threshold out of the total number of events under options 2, 3-1, and 4. The trends are almost the same, and the difference in the ratios is within 1%. The muon generator, thickness, length, and width of the PS strip were the same for the three configurations, and the declining trend of the event ratio was consistent for the three configurations. The black horizontal dotted line shows a proportion of 99%, from which it can be observed that the track length threshold of the corresponding black vertical dotted line is 3 mm. A total of 1% muon of events occurred in which the track length in the PS strip was <3 mm. Because the thickness of the PS is 20 mm, it is certain that these muon events are incident at a large zenith angle and pass through the edge of the PS, which is often referred to as an edge event. Therefore, if a PS module is built to stagger the PS up, down, left, and right, these edge events should also leave longer tracks on the next layer or the PS next to them so as to be triggered. Consequently, for a PS strip, the edge event may not be tagged (detected), but it may be tagged for the entire veto module system. Therefore, at the same threshold, the muon tagging efficiency of a single-layer module was higher than that of a single PS strip. From this perspective, the JUNO-TAO top veto system (TVT) was designed.

(a)

(b)
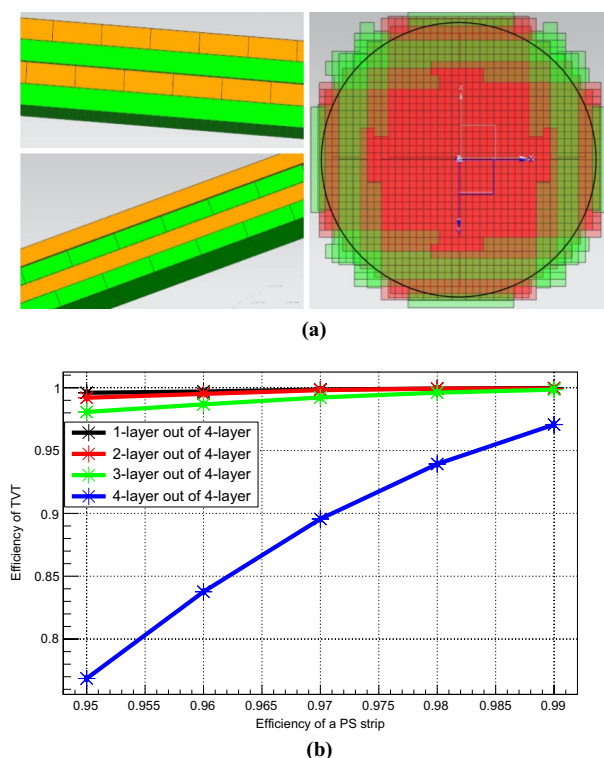
Fig. 15 (Color online) **a** Design of the JUNO-TAO TVT. The left panel is a side view. The right panel is a top view. **b** Muon tagging efficiency of hitting multilayer PSs compared with that of a single-layer PS

4 Performance of the JUNO-TAO TVT

Figure 15a shows the design scheme of the TVT. The left panel of Fig. 15a shows a side view of the whole four-layer PS, where the seam of the upper PS layer corresponds to the volume of the next PS layer, which can eliminate dead space. Simultaneously, the track direction of a muon can be determined using this system. Therefore, a four-layer PS was designed, and the gap between the neighboring layers was 2 cm. (This refers to the gap between the SiPM ends of one PS and another PS.) The right panel of Fig. 15a shows a top view of the whole four-layer PS. Different colors represent different PS layers. Because the central detector of the TAO is a ball, to reduce cost and consumables, we covered the ball's projection surface with the area of the PS, resulting in the formation of a circle with four layers.

Figure 15b shows the distributions of the muon tagging efficiency when hitting multilayer PSs versus that of a single PS. Different colors represent the efficiencies of hitting different numbers of PS layers. The black line represents the muon tagging efficiency of any of the four layers. Red indicates any two of the four layers. Because the gap between each layer is very small, the red and black lines almost coincide with the efficiency of the PS strip. The blue color

represents muons that hit all four layers and are tagged by the four layers of the PS. Because each layer has a certain dead space, as the efficiency of the PS strip decreases, the reduction in tagging efficiency in all four layers is the most noticeable. Green represents any three out of four layers, from which this conclusion can be obtained: Even if the efficiency of a PS strip is as low as 97%, which is equivalent to the threshold of 10 as shown in Table 3, the muon tagging efficiency of any three out of four layers will still be >99%. In addition, by simulating the environmental background (including ^{238}U, ^{232}Th, and ^{40}K chains), the background event rate that can pass the 3 p.e. threshold in any two out of four layers of the PS is 1280 ± 40 Hz, and the rate that can pass the 3 p.e. threshold in any three out of four layers of the PS is <10 Hz. Therefore, a condition can be selected in which any three of the four layers are triggered to tag muons and reject the background.

5 Summary

There are numerous PSs with WLS fiber options in different configurations. In this study, by using a simulation package, the differences between different configurations (e.g., the influence of the optical fiber diameter, layout, and other factors) on transmission performance were checked in detail. Based on the light yield and muon tagging efficiency, the optimal configuration of a WLS fiber PS was obtained under certain conditions. The relevant bench tests of options 1 and 4 were measured in terms of the most probable SiPM output, and the summed signal at one end of the optimized option 4 was ~32 p.e. The light yield was a factor of 4 greater than that of option 1, which further verified the reliability of the simulation package.

Simultaneously, inefficient muon events were studied. Finally, a design scheme for the JUNO-TAO TVT system was presented. The following conclusions can be given based on the simulation: Assuming 40% SiPM PDE, the muon tagging efficiency of a single PS strip at a 3 p.e. threshold can still reach 99% in the AND mode (i.e., when signals above the threshold are required from two sides of a PS strip), and the background event rate that can pass the threshold in any three of the four layers of the PS is <10 Hz (i.e., almost zero). When the threshold is 10 p.e., the muon tagging efficiency of a single PS strip is 97%; the efficiency of three layer out of four layer of TVT will still be >99%.

Declarations

Conflict of interest The authors declare that they have no competing interests.

References

1. P.A. Zyla, Particle Data Group, Review of particle physics. Prog. Theor. Exp. Phys. **08**, 08 (2020). https://doi.org/10.1093/ptep/ptaa104

2. M.Y. Guan, M.-C. Chu, J. Cao et al., A parametrization of the cosmic-ray muon flux at sea-level. https://doi.org/10.48550/arXiv.1509.06176

3. C. Patrignani, Particle Data Group et al., Review of particle physics. Chin. Phys. C **40**, 100001 (2016). https://doi.org/10.1088/1674-1137/40/10/100001

4. Z.Y. Guo, L. Bathe-Peters, S.M. Chen, (JNE Collaboration) et al., Muon flux measurement at China Jinping Underground Laboratory. Chin. Phys. C **45**, 025001 (2021). https://doi.org/10.1088/1674-1137/abccae

5. E. Barbuto, C. Bozza, M. Cozzi et al., Atmospheric muon flux measurements at the external site of the Gran Sasso Lab. Nucl. Instrum. Methods Phys. Res. Sect. A **525**, 485–495 (2004). https://doi.org/10.1016/j.nima.2004.01.078

6. W.H. Trzaska, M. Slupecki, L. Bandac et al., Cosmic-ray muon flux at Canfranc Underground Laboratory. Eur. Phys. J. C **79**, 721 (2019). https://doi.org/10.1140/epjc/s10052-019-7239-9

7. JUNO Collaboration, JUNO physics and detector. Prog. Part. Nucl. Phys. **123**, 0146–6410 (2022). https://doi.org/10.1016/j.ppnp.2021.103927

8. JUNO Collaboration and T. Adam et al., JUNO conceptual design report. physics.ins-det. https://ui.adsabs.harvard.edu/abs/2015arXiv150807166A

9. JUNO Collaboration and Angel Abusleme et al., TAO conceptual design report: a precision measurement of the reactor antineutrino spectrum with sub-percent energy resolution. physics.ins-det. https://ui.adsabs.harvard.edu/abs/2020arXiv200508745J

10. E. Aprile, F. Agostini, M. Alfonsi, XENON1T Collaboration, Conceptual design and simulation of a water Cherenkov muon veto for the XENON1T experiment. JINST **9**, P11006 (2014). https://doi.org/10.1088/1748-0221/9/11/P11006

11. E. Aprile, J. Aalbers, F. Agostini, XENON Collaboration, Projected WIMP sensitivity of the XENONnT dark matter experiment. J. Cosmol. Astropart. Phys. **2020**, 031 (2020). https://doi.org/10.1088/1475-7516/2020/11/031

12. M. Christmann, P. Achenbach, S. Aulenbacher et al., Light dark matter searches with DarkMESA. PoS, EPS-HEP2021, 398, 129 (2022). https://pos.sissa.it/398/129. https://doi.org/10.22323/1.398.0129

13. T. Alexander, D. Alton, K. Arisaka et al., DarkSide search for dark matter. JINST **8**, C11021 (2013). https://doi.org/10.1088/1748-0221/8/11/C11021

14. A. Pocar, EXO-200, nEXO collaboration, Searching for neutrino-less double beta decay with EXO-200 and nEXO. Nucl. Part. Phys. Proc. **265–266**, 42–44 (2015). https://doi.org/10.1016/j.nuclphysbps.2015.06.011

15. D. Tosi, EXO collaboration, Search for double beta decay with EXO-200. AIP Conf. Proc. **1560**, 187–189 (2013). https://doi.org/10.1063/1.4826749

16. R. Gornea, EXO-200 collaboration, Double beta decay in liquid xenon. J. Phys. Conf. Ser. **179**, 012004 (2009). https://doi.org/10.1088/1742-6596/179/1/012004

17. J.B. Birks, The theory and practice of scintillation counting (1964). https://www.slac.stanford.edu/spires/find/books

18. Y. Zhezher, Telescope Array collaboration, Study of muons in Ultra-High-Energy cosmic-ray air showers with the telescope array experiment. Phys. Atom. Nucl. **82**, 685–688 (2019). https://doi.org/10.1134/S1063778819660517

19. A. Erhart, NUCLEUS collaboration, Development of an organic plastic scintillator based muon veto operating at sub-kelvin temperatures for the NUCLEUS experiment, in *19th International Workshop on Low Temperature Detectors*. https://doi.org/10.1007/s10909-022-02842-5

20. J.W. Seo, E.J. Jeon, W.T. Kim et al., A feasibility study of extruded plastic scintillator embedding WLS fiber for AMoRE-II muon veto. Nucl. Instrum. Methods A **1039**, 167123 (2022). https://doi.org/10.1016/j.nima.2022.167123

21. K.J. Thomas, E.B. Norman, A.R. Smith et al., Installation of a muon veto for low background gamma spectroscopy at the LBNL low-background facility. Nucl. Instrum. Methods Phys. Res. Sect. A **724**, 47–53 (2013). https://doi.org/10.1016/j.nima.2013.05.034

22. A. Pla-Dalmau, A.D. Bross, K.L. Mellott, Low-cost extruded plastic scintillator. Nucl. Instrum. Methods A **466**, 482–491 (2001). https://doi.org/10.1016/S0168-9002(01)00177-2

23. A.A. Moiseev, P.L. Deering, R.C. Hartman et al., High efficiency plastic scintillator detector with wavelength-shifting fiber readout for the GLAST large area telescope. Nucl. Instrum. Methods A **583**, 372–381 (2007). https://doi.org/10.1016/j.nima.2007.09.040

24. V.M. Thakur, A. Jain, P. Ashokkumar et al., Design and development of a plastic scintillator based whole body beta/gamma contamination monitoring system. Nucl. Sci. Tech. **32**, 47 (2021). https://doi.org/10.1007/s41365-021-00883-1

25. U. Holm, K. Wick, Radiation stability of plastic scintillators and wave length shifters. IEEE Trans. Nucl. Sci. **36**, 579–583 (1989). https://doi.org/10.1109/23.34504

26. C. Bloise, S. Ceravolo, F. Cervelli et al., Design, assembly and operation of a Cosmic Ray Tagger based on scintillators and SiPMs. Nucl. Instrum. Methods A **1045**, 167538 (2023). https://doi.org/10.1016/j.nima.2022.167538

27. P. Buzhan, A. Karakash, Hand-foot monitors for nuclear plants based on scintillator–WLS–SiPM technology. J. Phys Conf. Ser. **1689**, 012011 (2020). https://doi.org/10.1088/1742-6596/1689/1/012011

28. W. Bugg, Yu. Efremenko, S. Vasilyev, Large plastic scintillator panels with WLS fiber readout; optimization of components. Nucl. Instrum. Methods A **758**, 91–96 (2014). https://doi.org/10.1016/j.nima.2014.05.055

29. J.N. Dong, Y.L. Zhang, Z.Y. Zhang et al., Position-sensitive plastic scintillator detector with WLS-fiber readout. Nucl. Sci. Tech. **29**, 117 (2018). https://doi.org/10.1007/s41365-018-0449-2

30. Y. Yang, C.P. Yang, J. Xin et al., Performance of a plastic scintillation fiber dosimeter based on different photoelectric devices. Nucl. Sci. Tech. **32**, 120 (2021). https://doi.org/10.1007/s41365-021-00965-0

31. T. Adam et al., The OPERA experiment target tracker. Nucl. Instrum. Methods A **577**, 523–539 (2007). https://doi.org/10.1016/j.nima.2007.04.147

32. P. Adamson, K. Alexandrov, G. Alexeev et al., The MINOS scintillator calorimeter system. IEEE Trans. Nucl. Sci. **49**, 861–863 (2002). https://doi.org/10.1109/TNS.2002.1039579

33. Y.P. Wang, C. Hou, X.D. Sheng et al., Testing and analysis of the plastic scintillator units for LHAASO-ED. Rad. Det. Tech. Meth. **54**, 513–519 (2021). https://doi.org/10.1007/s41605-021-00274-5

34. F. Aharonian, Q. An, Axikegu et al., Performance test of the electromagnetic particle detectors for the LHAASO experiment. Nucl. Instrum. Methods A. **1001**, 165193 (2021). https://doi.org/10.1016/j.nima.2021.165193

35. J. Evans, MINOS collaboration, The MINOS experiment: results and prospects. Adv. High Energy Phys. **2013**, 182537 (2013). https://doi.org/10.1155/2013/182537

36. S. Orsi, PAMELA collaboration, PAMELA: a payload for antimatter matter exploration and light nuclei astrophysics. Nucl. Instrum. Methods A **580**, 880–883 (2007). https://doi.org/10.1016/j.nima.2007.06.051

37. V. Andreev, V. Balagura, B. Bobchenko et al., A high granularity scintillator hadronic-calorimeter with SiPM readout for a linear collider detector. Nucl. Instrum. Methods A **540**, 368–380 (2005). https://doi.org/10.1016/j.nima.2004.12.002

38. D.J. Thompson, C.A. Wilson-Hodge, Fermi gamma-ray space telescope. arXiv:2210.12875

39. S. Procureur, Muon imaging: principles, technologies and applications. Nucl. Instrum. Methods Phys. Res. Sect. **878**, 169–179 (2018). https://doi.org/10.1016/j.nima.2017.08.004

40. K. Morishima, M. Kuno, A. Nishio et al., Discovery of a big void in Khufu's Pyramid by observation of cosmic-ray muons. Nature **552**, 386–390 (2017). https://doi.org/10.1038/nature24647

41. A. Zenoni, Historical building stability monitoring by means of a cosmic ray tracking system, in *4th International Conference on Advancements in Nuclear Instrumentation Measurement Methods and their Applications. IEEE Nuclear Science Symposium Conference Record*, pp. 1–8 (2015). https://doi.org/10.1109/ANIMMA.2015.7465542

42. J. Marteau, D. Gibert, N. Lesparre et al., Muons tomography applied to geosciences and volcanology. Nucl. Instrum. Methods A **695**, 23–28 (2012). https://doi.org/10.1016/j.nima.2011.11.061

43. S. Oguri, Y. Kuroda, Y. Kato et al., Reactor antineutrino monitoring with a plastic scintillator array as a new safeguards method. Nucl. Instrum. Methods A **757**, 33–39 (2014). https://doi.org/10.1016/j.nima.2014.04.065

44. A.Sh. Georgadze, V.M. Pavlovych, O.A. Ponkratenko et al., A remote reactor monitoring with plastic scintillation detector. arXiv:1610.05884

45. P.R. Scovell, A. Vacheret, A. Baird et al., Low background antineutrino monitoring with an innovative composite solid scintillator detector, in *2013 IEEE Nuclear Science Symposium and Medical Imaging Conference and Workshop on Room-Temperature Semiconductor Detectors*, pp. 1–7 (2013). https://doi.org/10.1109/NSSMIC.2013.682954

46. F. Capozzi, E. Lisi, A. Marrone, Mapping reactor neutrino spectra from TAO to JUNO. Phys. Rev. D **102**, 056001 (2020). https://doi.org/10.1103/PhysRevD.102.056001

47. S. Agostinelli, J. Allison, K. Amako et al., Geant4-a simulation toolkit. Nucl. Instrum. Methods Phys. Res. Sect. A **506**, 250–303 (2003). https://doi.org/10.1016/S0168-9002(03)01368-8

48. S. Riggi, P. La Rocca, E. Leonora et al., Geant4 simulation of plastic scintillator strips with embedded optical fibers for a prototype of tomographic system. Nucl. Instrum. Methods A **624**, 583–590 (2010). https://doi.org/10.1016/j.nima.2010.10.012

49. W.Z. Xu, Y.F. Liu, Z.Q. Tan et al., Geant4 simulation of plastic scintillators for a prototype uSR spectrometer. Nucl. Sci. Tech. **24**, 4 (2013). https://doi.org/10.13538/j.1001-8042/nst.2013.04.011

50. P. Lecoq, Scintillation detectors for charged particles and photons, in *Particle Physics Reference Library* (Springer, Cham, 2020), pp. 45–89 . https://doi.org/10.1007/978-3-030-35318-6-3

51. M. Li, Z.M. Wang, C.M. Liu et al., Performance of compact plastic scintillator strips with wavelength shifting fibers using a photomultiplier tube or silicon photomultiplier readout. Nucl. Sci. Tech. **34**, 2 (2023). https://doi.org/10.1007/s41365-023-01175-6

52. H. Yang, G. Luo, T. Yu et al., MuGrid: a scintillator detector towards cosmic muon absorption imaging. Nucl. Instrum. Methods A **1042**, 167402 (2022). https://doi.org/10.1016/j.nima.2022.167402

53. Hoton Technology Co. Beijing Hoton Nuclear Technology Co., Ltd. http://www.hoton.com.cn/English/index.html

54. C. Tur, V. Solovyev, J. Flamanc et al., Temperature characterization of scintillation detectors using solid-state photomultipliers for radiation monitoring applications. Nucl. Instrum. Methods A **620**, 351–358 (2010). https://doi.org/10.1016/j.nima.2010.03.141

55. E. Dietz Laursonn, Detailed studies of light transport in optical components of particle detectors. Aachen, Tech. Hochsch. https://inspirehep.net/literature/1505685

56. X.L. Qian, H.Y. Sun, C. Liu et al., Simulation study on performance optimization of a prototype scintillation detector for the GRANDProto35 experiment. Nucl. Sci. Tech. **32**, 51 (2021). https://doi.org/10.1007/s41365-021-00882-2

57. T. Gaisser, Cosmic-ray showers reveal muon mystery. APS Phys. **9**, 125 (2016). https://doi.org/10.1103/Physics.9.125

58. P. Shukla, S. Sankrith, Energy and angular distributions of atmospheric muons at the Earth. Int. J. Mod. Phys. A **33**, 1850175 (2018). https://doi.org/10.1142/S0217751X18501750

59. Semiconductor Components Industries, LLC. Cherry Semiconductor (1999–2023)